12-2012

Widely Tunable High-Efficiency Power Amplifier With Ultra-Narrow Instantaneous Bandwidth

Kenle Chen
Birck Nanotechnology Center, Purdue University, chen314@purdue.edu

Xiaoguang Liu
Birck Nanotechnology Center, Purdue University, lxgliu@ucdavis.edu

Dimitrios Peroulis
Birck Nanotechnology Center, Purdue University, dperouli@purdue.edu

Widely Tunable High-Efficiency Power Amplifier With Ultra-Narrow Instantaneous Bandwidth

Kenle Chen, *Student Member, IEEE*, Xiaoguang Liu, *Member, IEEE*, and Dimitrios Peroulis, *Member, IEEE*

***Abstract*—This paper reports the first power amplifier (PA) that simultaneously achieves a very narrow instantaneous bandwidth (2%) while being tunable over a 38.5% frequency range (2.1–3.1 GHz) with a measured 50%–60% efficiency in the entire band. Such PAs are in great demand for realizing all-digital burst-mode transmitters that are expected to become critical for the future generation of wireless communication systems. Unlike state-of-the-art planar PAs that cannot simultaneously achieve a narrow bandwidth and high efficiency, the presented PA employs a widely tunable high-Q ($Q > 300$ over the tuning range) cavity resonator as the output matching network. Furthermore, the tunable multiband matching is performed for both the fundamental frequency and the second harmonic to ensure a high efficiency. The measured PA is implemented with a Cree GaN transistor, and it delivers an output power of $\geq$ 36 dBm at a gain of $\geq$ 10 dB. Two-tone testing is further conducted, indicating a good linearity of this PA with an output third-order intercept point greater than 48 dBm over the entire band. This design demonstrates, for the first time, that multiband burst-mode transmitters can be potentially built with widely tunable high-efficiency narrowband PAs.**

***Index Terms*—Evanescent-mode (EVA) cavity, GaN, high efficiency, matching network, narrowband, piezoelectric actuator, power amplifier (PA), quality factor, tunable resonator.**

I. Introduction

ALL-DIGITAL burst-mode transmitters have been recently proposed and demonstrated as an effective method to efficiently and linearly amplify the modern high peak-to-average-ratio (PAR) signals, e.g., long-term evolution (LTE) [1]–[4]. Unlike the conventional supply-modulated transmitters, e.g., envelope tracking (ET) and envelope elimination and restoration (EER), the digital transmitter entirely eliminates the analog part (supply modulator), while the signal's AM information is encoded into pulse widths, resulting in a quasi-constant-envelope input for the power amplifier (PA), and thus, a high efficiency [1], [2]. Such a transmitter relies heavily on a narrowband output filter to reconstruct the AM linearity. Nevertheless, the efficiency and linearity are degraded due to the rejection of the out-of-band quantization noise and pulse reflections on the transmission line (TL) between the PA and filter [1]. One possible solution for this issue is to employ a narrowband filter/resonator at the drain node of the PA's transistor [5], [6], as illustrated in Fig. 1(a).

Ideally, the resonator bandwidth needs to be as narrow as the signal bandwidth [1], typically <1%. However, narrowing the resonator bandwidth also degrades its in-band response, shown in Fig. 1(b), which eventually deteriorates the PA efficiency. Thus, a high unloaded quality factor (Q_u, determined by the internal loss term of the resonator) is essential for such a narrowband PA design, as illustrated in Fig. 1(c). The impact of the res-

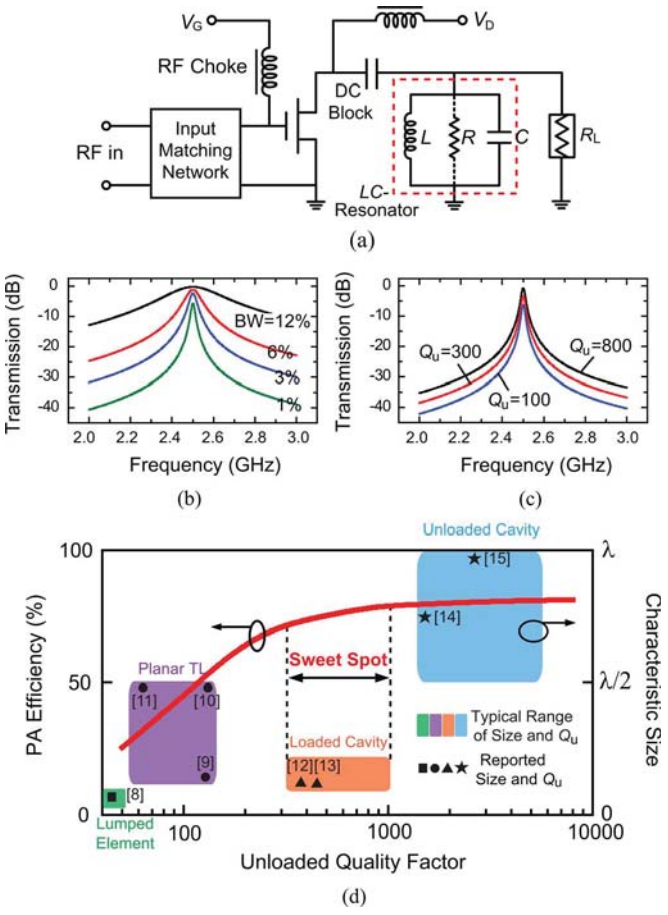

Fig. 1. (a) Typical PA topology with a narrowband resonator. (b) Effect of narrowing the bandwidth on resonator S_{21} with a constant $Q_u = 150$. (c) Effect of Q_u with a constant bandwidth of 1%. (d) PA efficiency versus resonator's Q_u of a narrowband design (BW $\approx 3\%$) [7] and different techniques for resonator implementation.

Manuscript received March 22, 2012; revised August 20, 2012; accepted August 22, 2012. Date of publication October 23, 2012; date of current version December 13, 2012. This work was supported by the Defense Advanced Research Projects Agency (DARPA) under the Purdue Microwave Reconfigurable Evanescent-Mode Cavity Filters Study.

K. Chen and D. Peroulis are with the School of Electrical and Computer Engineering and the Birck Nano Technology Center, Purdue University, West Lafayette, IN 47906 USA (e-mail: chen314@purdue.edu; dperouli@purdue.edu).

X. Liu was with the School of Electrical and Computer Engineering and the Birck Nano Technology Center, Purdue University, West Lafayette, IN 47906 USA. He is now with the Department of Electrical and Computer Engineering, University of California at Davis, Davis, CA 95616 USA (e-mail: lxgliu@ucdavis.edu).

Color versions of one or more of the figures in this paper are available online at http://ieeexplore.ieee.org.

Digital Object Identifier 10.1109/TMTT.2012.2220561

TABLE I
PERFORMANCE COMPARISON WITH OTHER BAND-RECONFIGURABLE PAS

Ref.	Freq. (GHz)	Tuning Method	P_{out} (W)	Eff. (%)	Filtering Effect
[19]	0.9/1.5 /1.9/2.2	MEMS Switch	1.1−1.2	46−62	Moderate
[20]	0.9/1.8	PIN Diode	1	41−42	Low
[21]	0.9/1.8−2.1	Varactor Diode	0.5−0.6	32−55	Low
[22]	0.9/1.5/1.9	PIN Diode	8−10	61−65*	Moderate
[23]	1-1.9	Varactor Diode	9−10	64−79	Low
This Work	2.1−3.1	Piezo	4−5	50−60	Ultra High

* Power added efficiency.

onator's Q_u on PA efficiency and bandwidth has been studied in [7]. The efficiency versus Q_u of a narrowband (3%) PA design is qualitatively illustrated in Fig. 1(d). Fig. 1(d) also exhibits the typical ranges of the quality factor and characteristic size of various microwave-resonator types, such as lumped elements [8], planar TLs [9]–[11], and 3-D cavities [12]–[15]. It is worth noting that the conventional lumped elements or planar TLs are not suitable for realizing narrowband high-efficiency PAs due to their inherently low Q_u. Among those techniques, the highly loaded [evanescent mode (EVA)] cavity yields an optimal option for realizing the narrowband PA in terms of size and performance, as shown in Fig. 1(d). Besides the high quality factors (300–1000) demonstrated in [12], [13], [16], and [17], the EVA cavity resonators also exhibit very large spurious-free regions, and they are widely tunable (>2:1) by employing various tuning methods [13], [16], [17]. More importantly, the EVA cavity can be directly integrated on the same substrate as the PA [13], [16]. Those characteristics make this integrated design particularly practical.

In [7], the design concept of a static narrowband PA integrated with a static EVA resonator was experimentally demonstrated at a single frequency of 1.27 GHz with ≈3% bandwidth. In this research, we extend the authors' previous work to the PA with a tunable output EVA resonator and increase the operating frequency to the S-band. This paper presents, for the first time, a band-reconfigurable PA with ultrahigh output frequency selectivity (≈2% bandwidth) and 38.5% frequency tuning range. Tuning is realized with an integrated piezoelectric actuator [16], [18], and the optimized matching is performed for both the fundamental frequency and the second harmonic over the entire tuning range. Large-signal measurement exhibits an efficient performance of the implemented PA, which compares favorably to those of the reported band-reconfigurable PAs [19]–[23], as presented in Table I. This design uniquely incorporates narrowband filtering in the output matching network and achieves switchless continuous tunability covering the entire 2.1–3.1-GHz band.

II. TRANSISTOR SELECTION AND CHARACTERIZATION

The 3-D illustration of the reconfigurable narrowband PA with a tunable EVA resonator is shown in Fig. 2. The cavity resonator is fabricated on the same substrate with the rest of the PA circuit, including the transistor, input matching network, and bias networks. The resonant frequency is sensitive to the gap distance between the sealing wall and the post (g). Thus, a

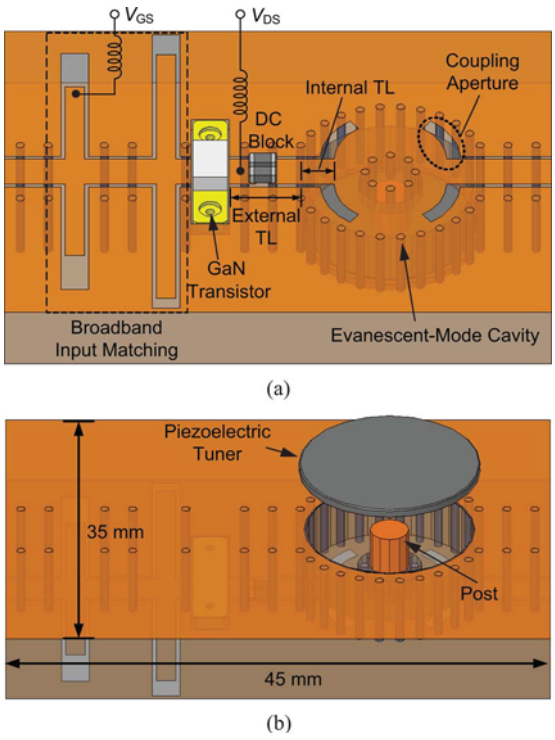

Fig. 2. 3-D illustration of the PA with a tunable EVA resonator. (a) Front side. (b) Back side with the tuner.

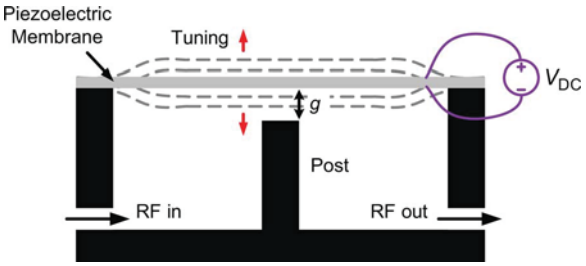

Fig. 3. Tuning mechanism of the reconfigurable EVA resonator.

piezoelectric actuator is integrated on the back side of the circuit board to change the PA's operation frequency, and the tuning mechanism is described in Fig. 3. By applying a bias voltage between the top and bottom surfaces of the piezoelectric actuator, the membrane moves toward the post or further away from it, changing the gap spacing, and thus the resonant frequency. In this investigation, a commercial 10-W GaN transistor (Cree CGH40010F) is selected as the RF power device. The nonlinear transistor model is provided by the manufacturer. The target frequency band is from 2 to 3 GHz, and the target 3-dB bandwidth is <3%.

To prescribe the desired input and output impedances of the transistor, load–pull and source–pull simulations are carried out with the manufacturer's model using Agilent Advanced Design System (ADS) [24]. Fig. 4(a) shows the extracted optimal input and output impedances of the transistor throughout the target band, where $Z_{L,\text{Opt.}}$ is optimized for efficiency and $Z_{S,\text{Opt.}}$ is optimized for power gain. Fig. 4(b) also shows Z_L contours that yield >70% drain efficiency from 2 to 3 GHz. It is seen that the Z_L contour moves in the counterclockwise direction as frequency is increased. The shaded area in Fig. 4(b) is the overlap of the contours across the 2–3-GHz band, which is the desired

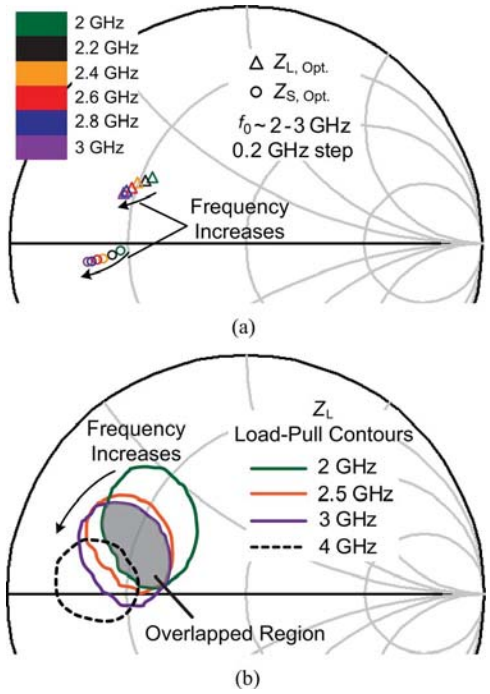

Fig. 4. Load–pull and source–pull simulation results of Cree GaN CGH40010F from 2 to 3 GHz. (a) Optimal load and source impedances. (b) Load impedance contours for >70% drain efficiency.

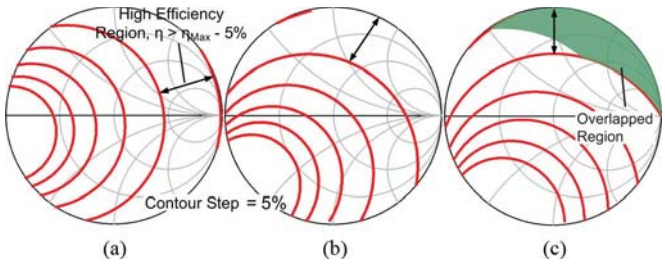

Fig. 5. Simulated load–pull contours of the second harmonic impedance: (a) at $2f_0 = 4$ GHz, (b) at $2f_0 = 5$ GHz, and (c) at $2f_0 = 6$ GHz showing the overlapped region from 2 to 3 GHz.

impedance region for the resonator's input port. As there is only one tuning freedom in this design, a large overlapped range is critical, which is described in Section III-B. The second harmonic matching is also considered in this multiband design, as it is very important for a high-efficiency PA design [26], [27]. Fig. 5 shows the second-harmonic contours from 2 to 3 GHz. The second harmonic impedance of the output resonator is desired to be located in the high-efficiency region indicated in Fig. 5(a)–(c). Fig. 5(c) shows the overlapped high-efficiency region throughout this band.

III. Design of Tunable EVA Resonator as the Output Matching Network

A. Quantified Impact of the Resonator's Q_u

In order to investigate the effect of Q_u on bandwidth and PA efficiency for this design, harmonic-balance (HB) simulation is performed with the simplified circuit model in Fig. 1(a) at 2.5 GHz, the center frequency of the target band. In this simulation, the load impedance Z_L is set to $Z_{L,\mathrm{Opt.}}$ obtained from the load–pull simulation, shown in Fig. 4(a). The HB simulation is

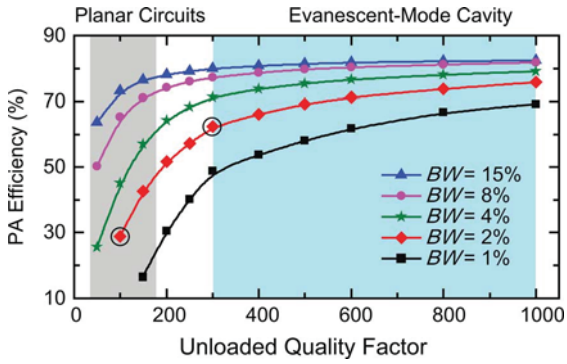

Fig. 6. Quantitative impact of resonator quality factor on bandwidth and PA efficiency, evaluated at 2.5 GHz with CHG40010.

conducted with a variable Q_u under different bandwidths from 1% to 15%. In each set of the simulations, constant bandwidth is maintained by selecting proper values of L and C, which are always resonant at 2.5 GHz. It can be seen from Fig. 6 that for the regular design with $\mathrm{BW} > 15\%$, a high PA efficiency of 75% can be achieved even using a low-Q resonator, e.g., $Q_u < 150$, as is commonly the case with planar printed circuit board (PCB)-based circuits [25]–[27]. However, as the bandwidth decreases, the advantage of using a high-Q_u resonator becomes much more significant, which leads to a greatly enhanced PA efficiency. Specifically, an effective doubling of the PA efficiency is achieved of the 2% BW PA design by increasing Q_u from 100 to 300, indicated by the circled points in Fig. 6. Therefore, the high-Q cavity resonators are particularly critical for implementing the narrowband high-efficiency PAs. Fig. 6 also underlines the most important tradeoffs between PA efficiency, bandwidth, and Q_u according to the specific requirements of the target system.

B. Output Matching Scheme Using the Strongly Coupled EVA Resonator

The EVA cavity resonator is a distributed implementation of the lumped-element resonator. Fig. 7(a)–(c) shows the geometry of a typical substrate-integrated EVA cavity [13], [18]. The electrical boundary of the cavity is defined by via-holes, and a post is placed at the center. The electromagnetic field is fed into the cavity using input and output coupling apertures. The shape of the slots are aligned with the direction of the magnetic field inside the cavity resonator. The electric field is predominantly concentrated in the gap between the post and the top membrane, which represents an effective capacitor; the magnetic field is truncated between the sidewall and the post, acting as a shorted coaxial line, which represents an effective inductor [13]. The unloaded quality factor (Q_u) of this resonator is inherently high because the E- and H-field are all distributed in air.

The circuit model of the EVA cavity resonator is shown in Fig. 8(a) [13], [18]. The value of C_r can be approximated by the equivalent capacitance formed by the post and top membrane, including parallel and fringing-field capacitances; the equivalent inductance L_r can be calculated following the model expressed in [13]; R accounts for the losses in the cavity resonator. The coupling structures are modeled as ideal transformers. The actual model of the EVA resonator contains an internal TL as

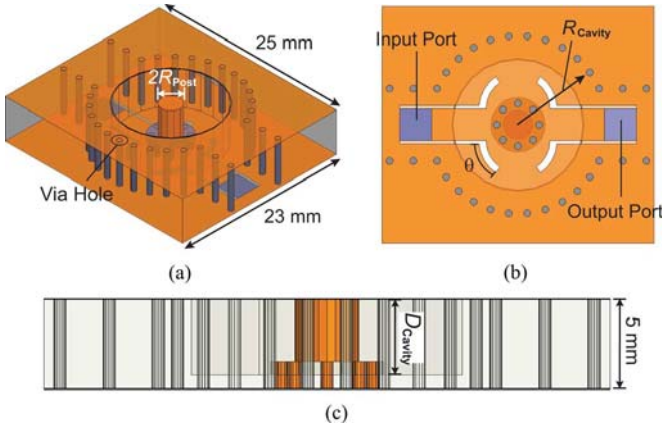

Fig. 7. Geometry of the EVA (HFSS model). (a) Top view. (b) Bottom view. (c) Side view.

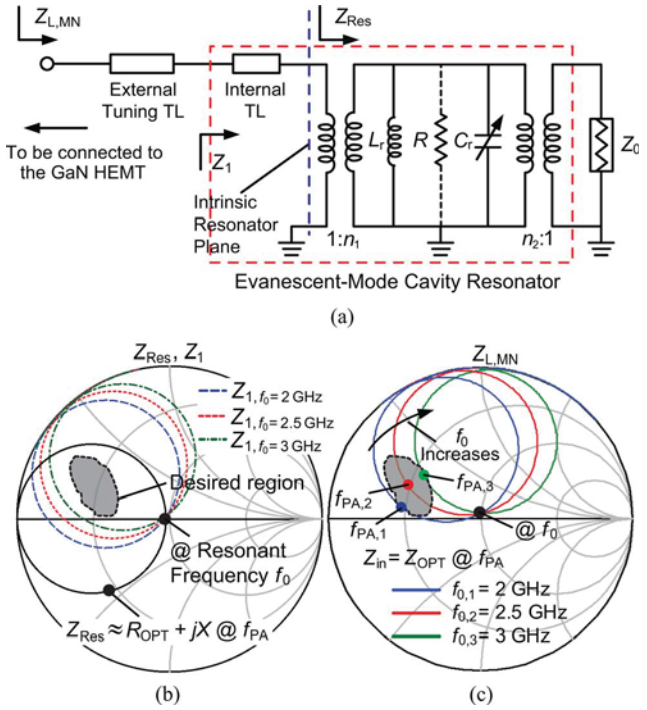

Fig. 8. Transistor output matching scheme using a strongly coupled tunable evanescent-model cavity resonator. (a) Circuit schematic. (b) Impedance of the intrinsic resonator $(Z_{\rm Res})$ and impedance of the actual resonator (Z_1) with $n_1 = n_2$. (c) Input impedance of the entire output matching network $(Z_{L,\rm MN})$.

the leading structure of the intrinsic resonator, which is also indicated in Fig. 2(a). Another external TL is connected at the resonator input to further tune the input impedance of the resonator to match the transistor output. The tunable resonator-matching-network design scheme is illustrated in Fig. 8.

For the intrinsic resonator, the input admittance $(Y_{\rm Res})$ can be expressed as

$$Y_{\rm Res} = \frac{n_1^2}{n_2^2}Y_0 + \frac{n_1^2}{R} + jn_1^2\left(\omega C_r - \frac{1}{\omega L_r}\right) \tag{1}$$

where n_1 and n_2 denote the input and output coupling coefficients, and Y_0 stands for the system admittance $(1/Z_0)$. The input impedance $Z_{\rm Res}(=1/Y_{\rm Res})$ moves along the constant-conductance circle $({\rm Re}(Y) = Y_0 \times n_1^2/n_2^2 + n_1^2/R)$ on the Smith chart when frequency varies. This is denoted by the red circular trajectory (in online version) in Fig. 8(b). For the special case of $n_1 = n_2$, this impedance is around Z_0 at the resonant frequency f_0 because the imaginary part is nullified and R is a very large value for a high-Q_u resonator. At a frequency slightly higher than f_0 (this will be the design frequency for the PA, $f_{\rm PA}$), $Z_{\rm Res}$ has the similar real part as the optimal impedance $Z_{L,\rm OPT.}$.

The $Z_{\rm Res}$ locus [red circle (in online version) in Fig. 8(b)] does not change as the resonator is tuned to different resonant frequencies. However, if a TL (or an inductor) is connected to in series the resonator, the resonator impedance moves clockwise and can be brought to $Z_{L,\rm OPT.}$, as described in Fig. 8(c). Here, $Z_{L,\rm MN}$ denotes the input impedance of the entire output matching network. As the resonant frequency changes, the $Z_{L,\rm MN}$ trajectories deviates from each other due to the effect of the internal and external TLs, shown in Fig. 8(c). However, by properly choosing the length of the external TL $({\rm TL_{EX}})$, the $Z_{L,\rm MN}$ trajectory can always be overlapped with the shaded region when f_0 varies from 2 to 3 GHz. Fig. 8(c) plots $Z_{L,\rm MN}$ trajectories with different f_0 values of 2, 2.5, and 3 GHz, respectively. Outside the 2–3-GHz band, there is no longer an overlap between $Z_{L,\rm MN}$ and the desired region because the $Z_{L,\rm MN}$ trajectory and load–pull contour (shown in Fig. 4) move in opposing directions versus frequency. Thus, the limitation of the tuning range is found to be around 1.5:1 using this approach with this transistor. A >1.5:1 tuning range may be achieved by incorporating an additional tuning freedom with a variable electrical length of the external TL or by employing a negative refractive index TL.

At the harmonic frequencies, the filter behavior of the resonator yields ideally a reflection coefficient of $|\Gamma| = 1$, leading to a rejection of the harmonic powers. The detailed design procedure is described step by step in Section III-C.

C. Design Procedure

Following the matching approach expressed in Fig. 8, the parameters incorporated in the output resonator design are determined in the following sequence.

1) *Initial Gap*: The initial gap g_0 between the post and top membrane is determined by the tuning ratio R_T and actuator displacement range d. As the piezoelectric membrane can be actuated bidirectionally, the dependence between R_T, d, and g_0 is given by

$$R_T \approx \sqrt{\frac{g_0 + d}{g_0 - d}} \Rightarrow g_0 \approx \frac{R_T^2 + 1}{R_T^2 - 1}d \tag{2}$$

where d denotes the maximum unidirectional deflection of the top membrane. The piezoelectric actuator (commercially available form Piezosystems Inc., Woburn, MA) used in this design is made by zirconate titanate, and it has a 0.38-mm thickness and 12.7-mm diameter. It can experimentally provide a unidirectional deflection of around 13 μm [16], depending on the attachment of the tuner. The dependence of deflection and bias voltage is presented in [13]. Equation (2) implies that a smaller initial gap g_0 leads to a larger tuning ratio. However, a smaller gap also worsens the power-handling capability due to the quasi-electrostatic force induced by the RF signal, as expressed in [28]. Thus, to achieve a 1.5:1 tuning ratio with the highest

TABLE II
FINAL CAVITY PARAMETERS

Cavity Radius R_{Cavity}	6.8 mm
Cavity Depth D_{Cavity}	4.2 mm
Post Radius R_{Post}	1.2 mm
Initial RF Gap g_0	30 μm
Simulated Q_{u}	460−680
Equivalent Inductance L_{r}	2.1 nH
Equivalent Initial Capacitance $C_{r,0}$	1.35 pF

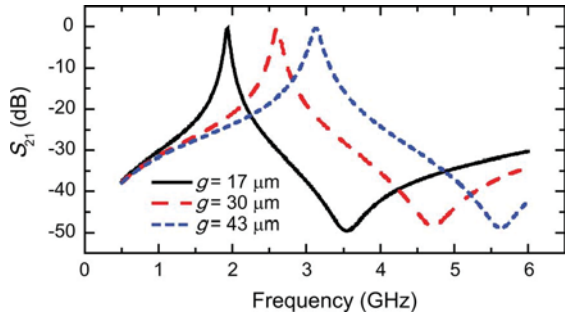

Fig. 9. Full-wave simulated S_{21} of the tunable resonator with various g.

possible power handling, the largest possible value of g_0 should be selected, which is approximately 30 μm, as calculated from (2).

2) *Cavity Dimensions*: The geometrical dimensions of the cavity (Fig. 7), including cavity radius (R_{Cavity}) and post radius (R_{Post}), determine the resonant frequency and unloaded quality factor. An EVA model with the typical dimensions presented in [13] and [16] is utilized in this design and simulated in Ansoft High Frequency Structure Simulator (HFSS) [29]. Specifically, the cavity size needs to match the size of the piezoelectric actuator for packaging considerations, as mentioned in [16]. R_{Post} is then optimized to cover the desired frequency range. The finalized dimensional parameters of the cavity are listed in Table II. Fig. 9 shows the simulated S_{21} of the resonator when g is tuned from 17 to 46 μm, indicating a frequency tuning range from 1.98 to 3.12 GHz. The simulated Q_u varies from 460 to 680 within this frequency range, which fulfills the requirements presented in Section III-A.

3) *Coupling Coefficients and TL Lengths*: The input and output coupling coefficients (n_1 and n_2) mainly determine the resonator bandwidth, and their initial values are identically set to $n_1 = n_2 = 6.5$ to result in a $\approx 2.5\%$ 3-dB bandwidth. The internal-TL length $(\mathrm{TL_{IN}})$ in Fig. 8 relates to the cavity size, which is given by $\mathrm{TL_{IN}} \approx 10$ mm as extracted from HFSS simulation. This length actually exceeds the desired value for performing the transistor matching using the scheme described in Fig. 8, requiring a negative external-TL length $(\mathrm{TL_{EX}})$ for tuning. However, the shortest $\mathrm{TL_{EX}}$ is around 2 mm to place the bias line and transistor leading pad. To compensate this effect, the input coupling is enhanced (decreasing n_1), which changes the Z_{Res} trajectory from the case with identical couplings, as illustrated in Fig. 10(a), leading to a more capacitive Z_{Res} at f_{PA}. Thus, a longer $\mathrm{TL_{EX}}$ is required to bring this impedance to the shaded region. The value of n_2 remains constant to maintain the bandwidth of the resonator, as indicated in Fig. 10(b). The optimized value

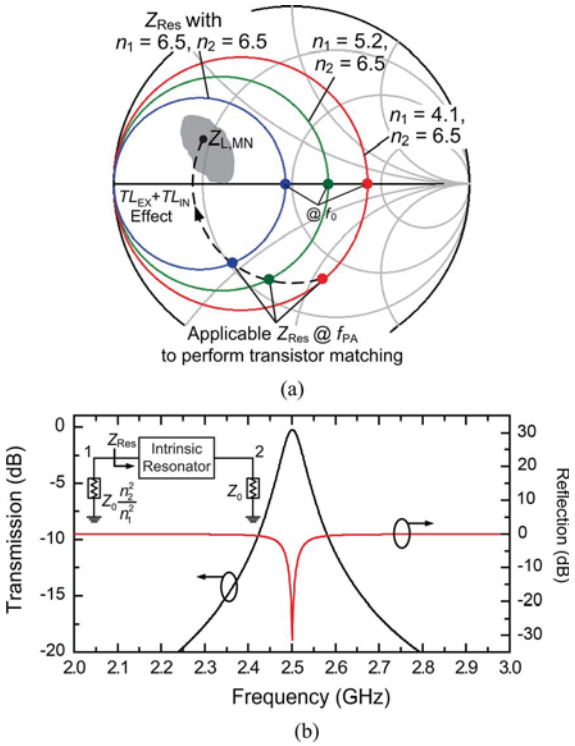

Fig. 10. Effect of changing the input coupling coefficient on: (a) input impedance of the intrinsic resonator (Z_{Res} in Fig. 8) and (b) frequency response of the resonator with a constant bandwidth of around 2.5%.

of n_1 is found from the circuit schematic simulation using ADS, given by $n_1 \approx 4.3$. Subsequently, the obtained n_1 and n_2 are transferred into the physical model using HFSS. As the coupling strength is predominantly determined by the length of the slot aperture, the input aperture length is larger than the output one for achieving a stronger coupling. The finalized coupling structures and the relevant dimensions are shown in Fig. 11(a). Fig. 11(b) shows the simulated $Z_{L,\mathrm{MN}}$ of the designed resonator with a variable g from 17 to 43 μm, indicating a good matching quality for the desired fundamental impedances throughout the target band.

4) *Bias Line and Harmonic Matching*: The dc-bias line needs to be added in order to supply the dc power to the transistor. As the feeding TL of the cavity is grounded at dc (by via-holes), a dc-block capacitor is needed to separate the transistor's drain and ground, as shown in Fig. 11(a). In the static design [7], the bias line is realized using a suspended conducting wire. In this design, the bias line is designed as a short-ended TL appended to the external TL in order to further tune the second harmonic impedance because the second-harmonic impedance, shown in Fig. 11(b), is not optimized (does not fall into the green-shaded region (in online version) at $2f_{\mathrm{PA}}$). A high-impedance bias TL (76 Ω) is chosen here with its length eventually determined by simulation aiming to tune the second harmonic impedance to the green overlapped region (in online version), while maintaining the fundamental impedance in the original gray-shaded region. The finalized bias-line length is 4.5 mm, shown in Fig. 11(a). The input impedance of the output resonator with the bias line is shown in Fig. 11(c),

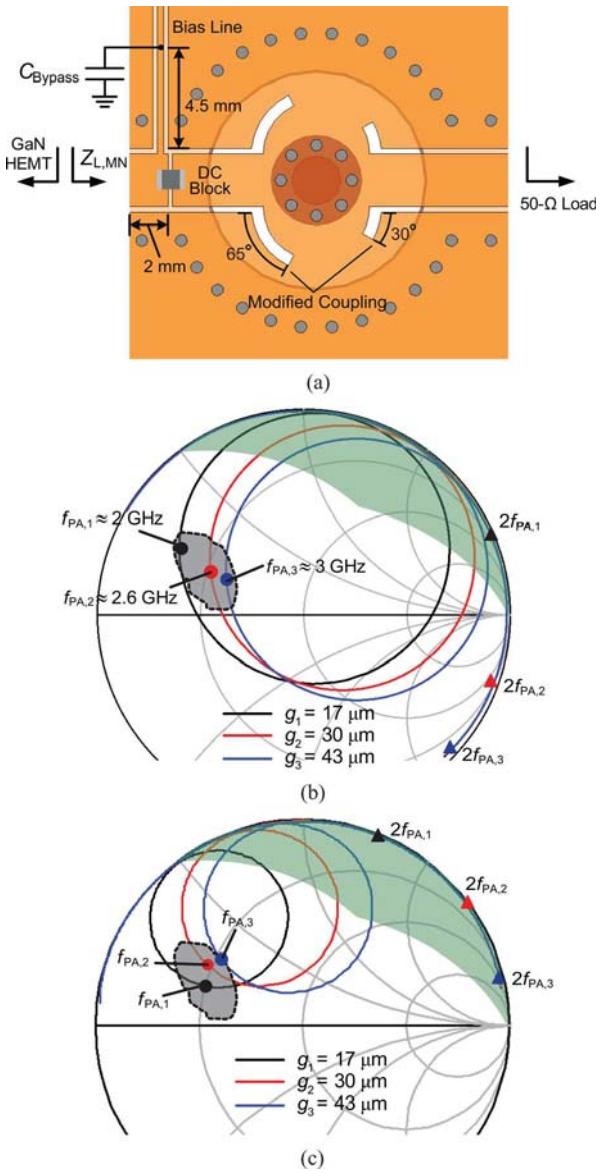

Fig. 11. Finalized design. (a) Entire output stage. (b) Simulated $Z_{L,\mathrm{MN}}$ without the bias line, (c) Simulated $Z_{L,\mathrm{MN}}$ with the bias line.

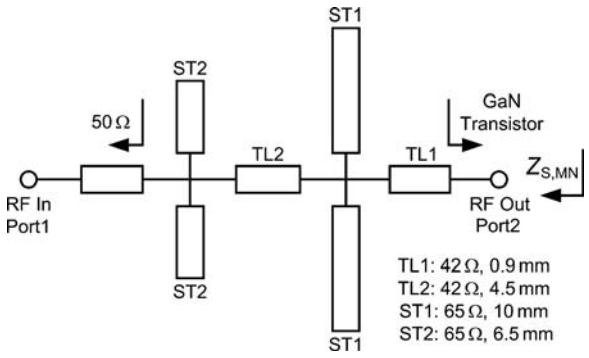

Fig. 12. Circuit schematic of the two-stage low-pass input matching network implemented using TL sections.

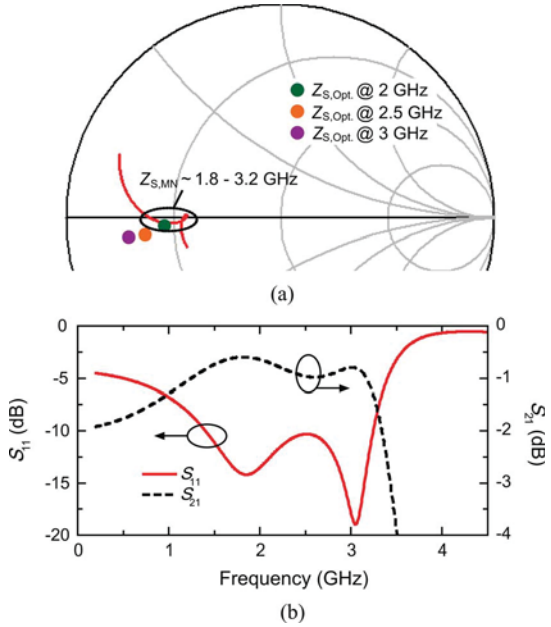

Fig. 13. Full-wave simulated results of the input matching network. (a) Output impedance at Port2. (b) S-parameters with Port1 and Port2 impedances of 50 Ω and $Z^*_{S,\mathrm{Opt.}}$ at $f_0 = 2.5$ GHz.

indicating that the desired matching is achieved for both the fundamental and second harmonic, leading to a quasi-saturated PA mode over the target band [30].

IV. PA Design and Fabrication

A. Input Matching Network Design

To match the input of the transistor across the 2–3-GHz band, a two-stage broadband low-pass matching network is designed. The synthesis and implementation of multistage low-pass matching networks for PA design has been well studied in detail in [27]. This design follows the same approach. The inductors are replaced by short TLs, and the capacitors are replaced by open-ended stubs (STs). Coplanar-waveguide (CPW) lines are used to build the TL sections of the input matching network. The circuit schematic is shown in Fig. 12. Full-wave simulation is performed for the input matching circuit using HFSS. Fig. 13(a) shows the simulated output impedance provided by this matching network. Fig. 13(b) shows the S-parameters with a 50-Ω termination at Port1 and a Port2 impedance of the conjugate of $Z_{S,\mathrm{Opt.}}$ at $f_0 = 2.5$ GHz (center frequency of the band).

B. Schematic Simulation of the Implemented PA Circuit

The entire circuit is created by connecting the GaN transistor to the input matching network and output resonator, and the schematic is shown in Fig. 14. The input bias network is composed of a 22-nH inductor in series with a 250-Ω resistor as the amplifier stabilizer. Simulation using manufacturer's models shows that this network yields an impedance of $|Z| > 300$ at a frequency higher than 2 GHz, which presents an effective open. Another 22-nH inductor is connected at the end of the output bias line to prevent RF power leakage. This circuit schematic is simulated using the HB simulator in ADS together with the cavity resonator model extracted from HFSS, and it is assumed that the large-signal response of the cavity resonators is the same as the small-signal response. Fig. 15 shows the simulated output power and efficiency versus frequency under a 26-dBm input stimulus, when g varies from 17 to 43 μm. Another set of simulations are carried out based on the circuit-schematic

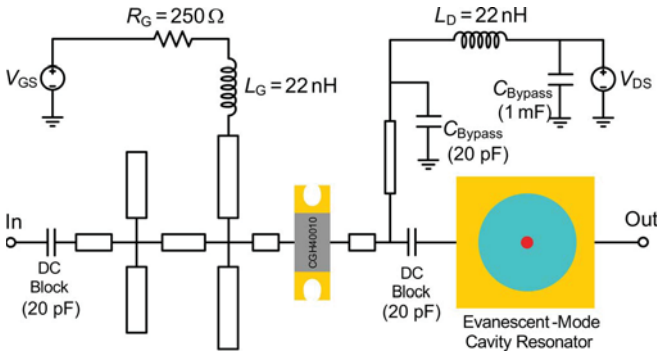

Fig. 14. Circuit schematic of the PA with a tunable EVA cavity resonator.

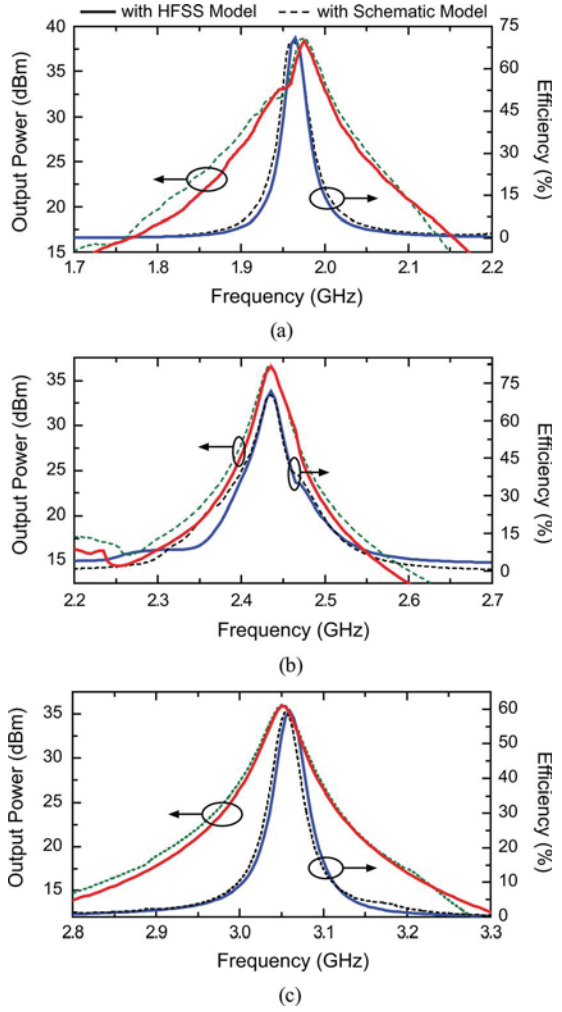

Fig. 15. Simulated output power and efficiency versus frequency. (a) $g = 17\,\mu$m, $C \approx 2.6$ pF. (b) $g = 26\,\mu$m, $C \approx 1.7$ pF. (c) $g = 43\,\mu$m, $C \approx 1.1$ pF.

model of cavity resonator (Fig. 8). Fig. 15 indicates a very good agreement between the simulation results of those two models.

C. Fabrication

The tunable PA module is fabricated in a single 5-mm Rogers TMM3 substrate. The front side and back side of the fabricated circuit are shown in Fig. 16(a) and (b). The transistor is soldered in a metallized slot cut into the substrate. The output tunable resonator fabrication follows a similar process with those of the standalone tunable filters in [13] and [16]. The EVA and the capacitive post are milled out inside the substrate. The electrical

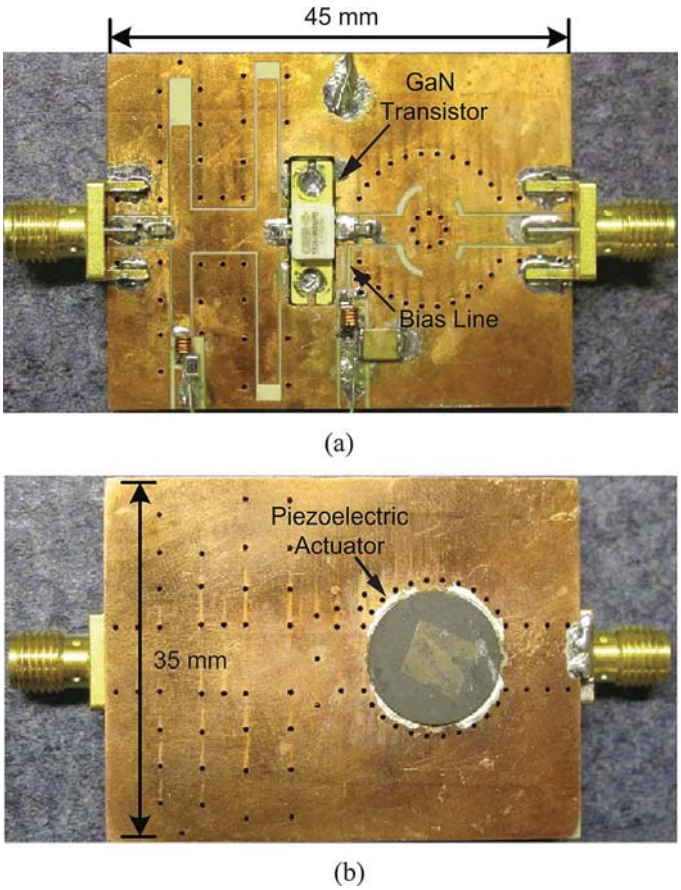

Fig. 16. Fabricated tunable PA-resonator module. (a) Front side. (b) Back side.

boundary of the cavity resonator is defined by copper-platted through-substrate vias. The lower surface of piezoelectric actuator is covered by a thin layer $(2\ \mu\text{m})$ of sputtered gold. The piezo actuator is attached to the substrate using silver epoxy.

V. Experimental Results

To experimentally evaluate the designed PA-resonator module, the fabricated device is measured under high-power stimulus. In the measurement, the transistor gate is biased at around the threshold of -3.3 V, and the drain is biased at 25 V. The bias voltage on the piezoelectric actuator varies from -150 to $+150$ V to produce $\approx \pm 13$-μm variation of the gap distance. In the real application, such high voltages can be supplied by integrated charge pumps [31], [32].

A. Continuous Wave (CW) Evaluation

To determine the actual frequency tuning range, the small-signal response of the implemented PA-resonator circuit is first measured using an Agilent E8361C performance network analyzer (PNA). The measured small-signal gain (S_{21}) is plotted in Fig. 17, indicating a tuning range from 2.1 to 3.2 GHz and $\cong$ 12-dB small-signal gain at the center frequency over this band.

Subsequently, a large-signal measurement is carried out within the same frequency band using the setup illustrated in Fig. 18. A commercial broadband PA (Mini-Circuits,

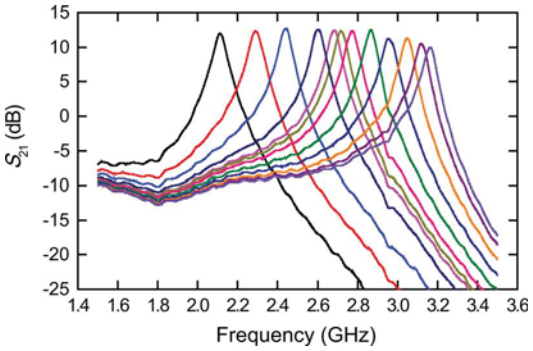

Fig. 17. Measured small-signal frequency response.

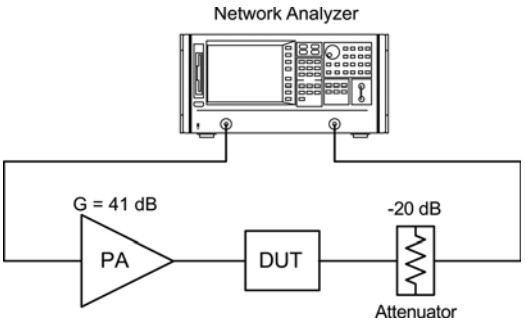

Fig. 18. Large-signal testing setup.

ZHL16W-43+, $\approx$ 16-W $P_{\mathrm{Max.}}$, $\approx$ 41-dB gain, 1.8–4 GHz[1]) is used to boost the input signal. The PA gain and attenuator's insertion loss are subtracted from the measured S_{21}. Fig. 19 shows the measured frequency responses under an input stimulus of 25 dBm, which is fed into the input port of the PA-resonator module. It is important to note that although only a selection of data points are shown in Figs. 17 and 19, the PA resonator is continuously tunable over the entire frequency range. It can also be seen that there is no bifurcation distortion in the measured large-signal response due to the quasi-electrostatic force induced by the high RF signal [28], [33]. It underlines that the piezoelectric tuner is capable of handling around 37-dBm output power over the entire band. A higher output power of up to 10 W may be achieved by reducing the tuning range, i.e., using a larger initial gap. Fig. 20 shows a summary of the small- and large-signal center-frequency gain and 3-dB bandwidth over the entire frequency band. The difference in gain between small- and large-signal results are mainly due to the gain-compression effect of the PA as the transistor is saturated. It is also seen from Fig. 20 that the measured 3-dB bandwidth is around 2%–3%, which fulfills the design target.

The input power is then swept from 7 to 28 dBm when the circuit is operating at a center frequency of $f_0 \cong 2.6$ GHz, and the measured frequency responses are shown in Fig. 21. The measured and simulated center-frequency gain and output power versus various input powers are plotted in Fig. 22, indicating that the gain starts to compress when P_{in} reaches 20 dBm. A good agreement can be seen between measurement and simulation. Fig. 22 also shows the simulated efficiency performance of the PA, indicating a maximum efficiency of around 68%.

[1]Mini-Circuits Corporation, Brooklyn, NY. [Online]. Available: http://www.minicircuits.com/

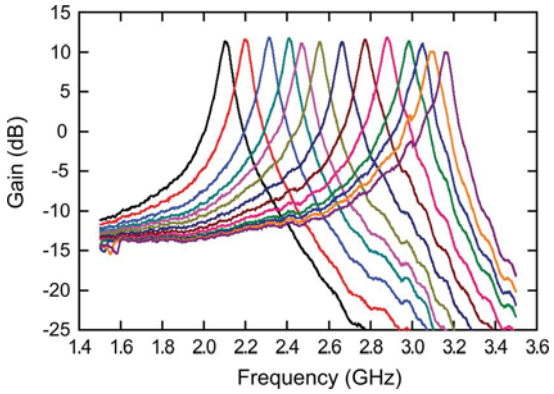

Fig. 19. Measured large-signal frequency response with 25-dBm input power.

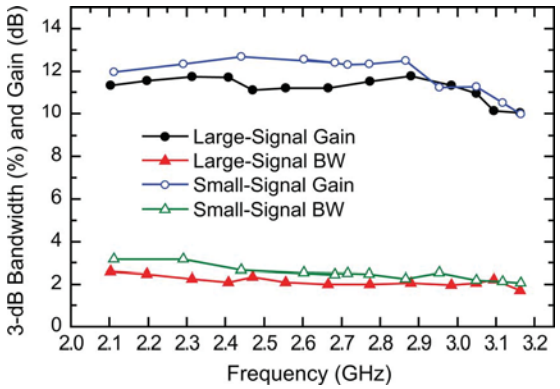

Fig. 20. Measured bandwidth and gain.

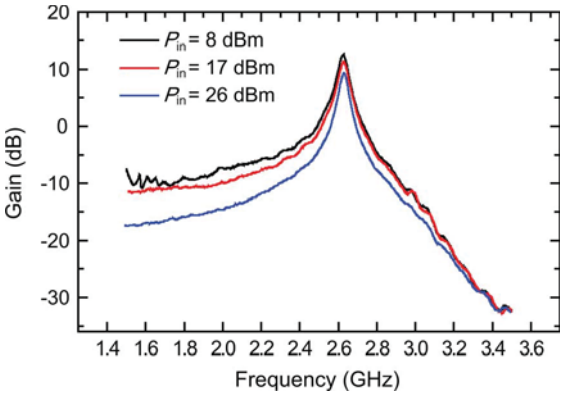

Fig. 21. Measured frequency response of gain under various power level.

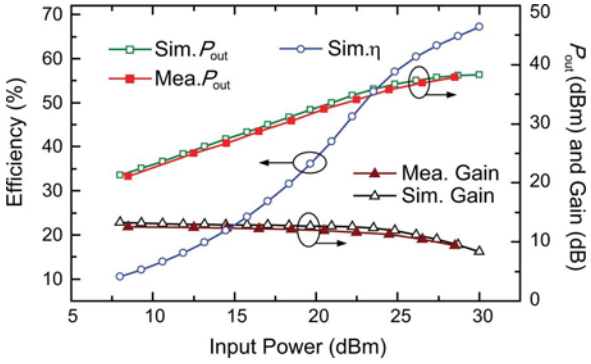

Fig. 22. Measured and simulated PA performance at $f_0 = 2.6$ GHz versus input power.

The PA circuit is also measured using a high-power CW testing setup to evaluate the overall efficiency, as shown in

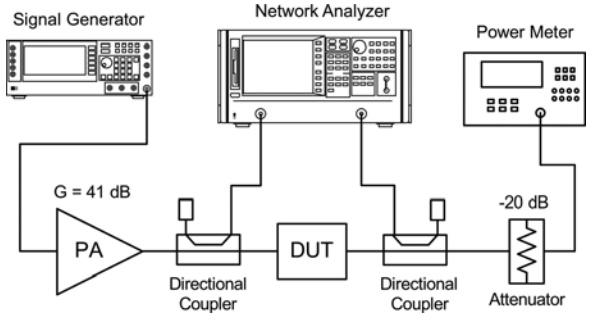

Fig. 23. High-power testing setup for CW evaluation on the tunable PA resonator.

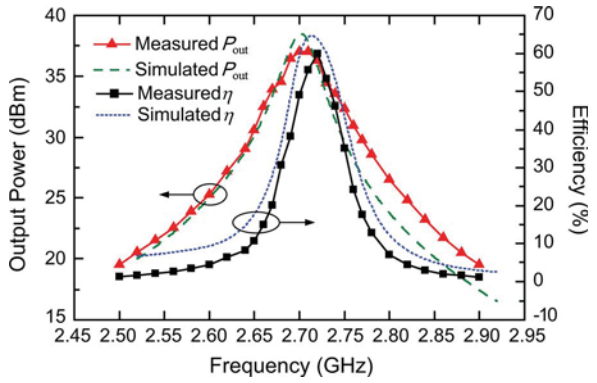

Fig. 24. Measured and simulated output power and efficiency under the stimulus of a frequency-swept 26-dBm CW signal.

Fig. 23. A CW signal is generated by an Agilent 4433B signal generator, and it is amplified by the ZHL-16W-43+ PA. The amplified signal is applied to the input of the tunable PA resonator through a 20-dB bidirectional coupler. The output signal is fed into the power meter through another coupler. The −20-dB coupling ports of the couplers are connected to the input and output ports of the PNA, enabling the detection of the instantaneous frequency response of the circuit module.

Fig. 24 shows the output power and overall efficiency when a 26-dBm input power is swept around a center frequency of $f_0 = 2.7$ GHz with a 0.4-GHz span. It is seen that the maximum output power is about 37 dBm and the maximum efficiency is around 62%. The CW measurement is then performed at various resonant frequencies (f_0) over the entire band. Fig. 25 shows the measured and simulated efficiency at f_0 and the corresponding output power under the stimulus of a 26-dBm input power within the entire frequency tuning range. An overall efficiency of around 50%–60%, power-added efficiency (PAE) of 41%–52%, and $P_{\rm out}$ of around 36.5 dBm are measured. Compared to the simulation results, the degradation of measured efficiency is mainly due to the use of silver epoxy as the bonding material, which has a much smaller conductivity compared to metals, e.g., gold and copper, leading to a reduction of Q_u [13]. A modified simulation is carried out again with a 30% reduction of Q_u, yielding a better agreement with the measurement, as shown in Fig. 25. Thus, it is estimated that the actual Q_u of the implemented resonator is around 70% of the simulated value.

B. Linearity Evaluation With Two-Tone Signal

The linearity performance of the tunable PA is evaluated using a two-tone signal. The measurement is first conducted

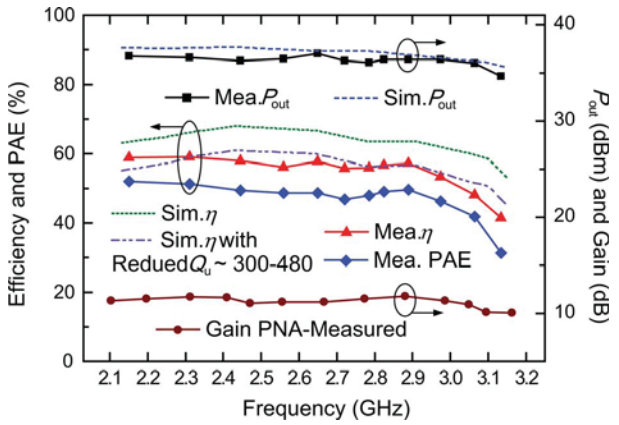

Fig. 25. Measured and simulated output power and efficiency across the entire band.

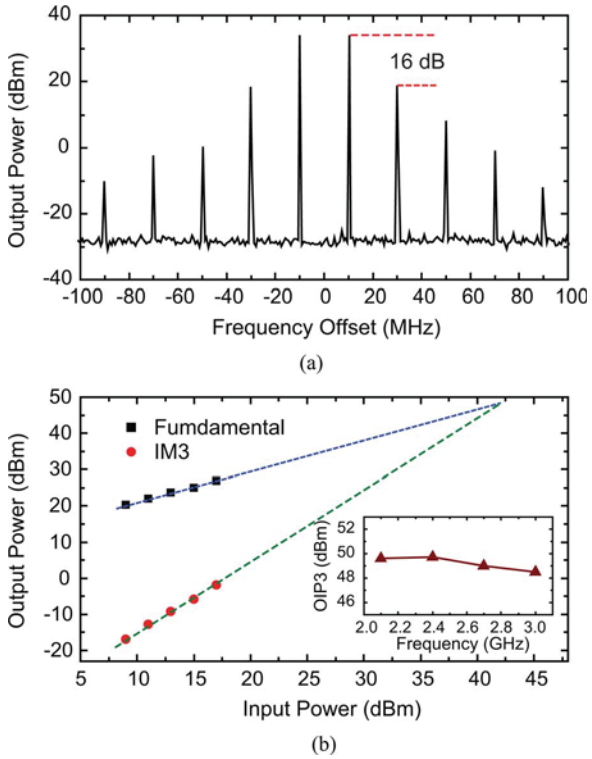

Fig. 26. Linearity measurement. (a) Output spectrum under the stimulus of a 25-dBm 20-MHz two-tone signal centered at 2.7 GHz. (b) Extraction of OIP3.

at 2.7 GHz. The separation of two tones is selected based on the passband of the narrowband PA, which is considered as the measured 1-dB bandwidth. Thus, a 20-MHz spacing is utilized at 2.7 GHz. Fig. 26(a) shows the captured output spectrum of the PA under a 25-dBm two-tone stimulus, indicating a third-order intermodulation (IM3) of −16 dBc at the saturated power level. The output third-order intercept point (OIP3) is extracted by varying the input power of the two-tone signal, as illustrated in Fig. 26, leading to a measured OIP3 of 49 dBm. The same experiment is then conducted at three different frequency points of 2.1, 2.4, and 3 GHz. The measured OIP3 is greater than 48 dBm over the entire tuning frequency range, as shown in the inset of Fig. 26(b). The measured results compare favorable to those of a reported linear PA design [34], indicating a good linearity performance of this PA. It is also important to note that the frequency separation of the two-tone

signal is much higher than the mechanical resonant frequency of the piezoelectric actuator, i.e., $<$ 5 kHz, as mentioned in [33], causing a negligible contribution to the intermodulation (IM) distortion induced by the vibration of the piezo membrane. Thus, the generation of IM products is solely due to the PA's nonlinear behavior.

VI. Conclusion

This paper has demonstrated, for the first time, a novel band-reconfigurable PA design that incorporates narrowband filtering at the output while achieving a high operating efficiency. These features are of great importance for the PAs in all-digital burst-mode transmitters. The key enabler of such a narrowband high-efficiency design is the utilization of high-Q EVA resonator as the output matching network. Furthermore, continuous frequency tunability is realized with an integrated piezoelectric actuator, and both the fundamental and second-harmonic matchings are performed to ensure high efficiency. Experimental results show that the implemented PA simultaneously achieves a very narrow bandwidth of $\approx$2% and a continuous tunability from 2.1 to 3.1 GHz, while maintaining an efficient PA performance of 50%–60% efficiency, $\geq$ 36-dBm output power, and $\geq$ 10-dB gain throughout this band. Moreover, the evaluation using a two-tone signal reveals a good linearity performance of this PA.

Acknowledgment

The authors would like to thank Dr. H. H. Sigmarsson, E. Naglich, and Dr. S. Moon, all with Purdue University, West Lafayette, IN, for helpful discussions and technical assistance. The authors are also grateful to Cree Inc., Durham, NC, for supplying the transistor model. The views expressed are those of the authors and do not reflect the official policy or position of the Department of Defense or the U.S. Government. Approved for Public Release, Distribution Unlimited.

References

[1] P. Reynaert, "Polar modulation," *IEEE Microw. Mag.*, vol. 12, no. 1, pp. 46–51, Jan. 2011.

[2] S. Blasubramanian, S. Boumaiza, H. Sarbishaei, T. Quach, P. Orlando, J. Volakis, G. Creech, J. Wilson, and W. Khalil, "Ultimate transmission," *IEEE Microw. Mag.*, vol. 13, no. 1, pp. 64–82, Jan. 2012.

[3] D. R. Parveg, P. Singerl, A. Wiesbauer, H. M. Nemati, and C. Fager, "A broadband, efficient, overdriven class-J RF power amplifier for burst mode operation," in *Proc. 40th Eur. Microw. Conf.*, Sep. 2010, pp. 1666–1669.

[4] E. Serebryakova, A. Samulak, K. Blau, and M. Hein, "Reconstruction filters for switch-mode power amplifier systems," in *Proc. 39th Eur. Microw. Conf.*, Oct. 2009, pp. 1453–1456.

[5] B. Francois, P. Reynaert, A. Wiesbauer, and P. Singerl, "Analysis of burst-mode RF PA with direct filter connection," in *Proc. 40th Eur. Microw. Conf.*, Sep. 2010, pp. 974–977.

[6] B. Francois, E. Kaymaksut, and P. Reynaert, "Burst mode operation as an efficiency enhancement technique for RF power amplifiers," in *IEEE USI Gen. Assembly Sci. Symp.*, Aug. 2011, pp. 1–4.

[7] K. Chen, X. Liu, W. J. Chappell, and D. Peroulis, "Co-design of power amplifier and narrowband filter using high-Q evanescent-mode cavity resonator as the output matching network," in *IEEE MTT-S Int. Microw. Symp. Dig.*, Jun. 2011, pp. 1–4.

[8] K. Entesari, K. Obeidat, A. R. Brown, and G. M. Rebeiz, "A 25–75-MHz RF MEMS tunable filter," *IEEE Trans. Microw. Theory Techn.*, vol. 55, no. 11, pp. 2399–2405, Nov. 2007.

[9] R. H. Geschke, B. Jokanovic, and P. Meyer, "Filter parameter extraction for triple-band composite split-ring resonators and filters," *IEEE Trans. Microw. Theory Techn.*, vol. 59, no. 6, pp. 1500–1508, Jun. 2011.

[10] S. Park, M. A. El-Tanani, I. Reines, and G. M. Rebeiz, "Low-loss 4–6-GHz tunable filter with 3-bit high-Q orthogonal bias RF-MEMS capacitance network," *IEEE Trans. Microw. Theory Techn.*, vol. 56, no. 10, pp. 2348–2355, Oct. 2008.

[11] K. Entesari and G. M. Rebeiz, "A 12–18-GHz three-pole RF MEMS tunable filter," *IEEE Trans. Microw. Theory Techn.*, vol. 53, no. 8, pp. 2566–2571, Oct. 2005.

[12] S. Park, I. Reines, C. Patel, and G. M. Rebeiz, "High-Q RF-MEMS 4–6-GHz tunable evanescent-mode cavity filter," *IEEE Trans. Microw. Theory Techn.*, vol. 58, no. 2, pp. 381–389, Feb. 2010.

[13] X. Liu, L. P. B. Katehi, W. J. Chappell, and D. Peroulis, "High-Q continuously tunable electromagnetic cavity resonators and filters using SOI-based RF MEMS actuators," *J. Microelectromech. Syst.*, vol. 19, no. 4, pp. 774–784, Jul. 2010.

[14] L. Harle and L. P. B. Linda, "A horizontally integrated micromachined filter," in *IEEE MTT-S Int. Microw. Symp. Dig.*, Jun. 2004, pp. 437–440.

[15] M. Stickel, G. V. Eleftheriades, and P. Kremer, "High-Q bulk micromachined silicon cavity resonator at $K\alpha$-band," *IET Electron. Lett.*, vol. 37, no. 7, pp. 433–435, Mar. 2001.

[16] S. Moon, H. H. Sigmarsson, H. Joshi, D. Peroulis, and W. J. Chappell, "Substrate integrated evanescent-mode cavity filter with a 3.5 to 1 tuning ratio," *IEEE Microw. Wireless Compon. Lett.*, vol. 20, no. 8, pp. 450–452, Aug. 2010.

[17] M. S. Arif, W. Irshad, X. Liu, W. J. Chappell, and D. Peroulis, "A high-Q magnetostatically-tunable all-silicon evanescent cavity resonator," in *IEEE MTT-S Int. Microw. Symp. Dig.*, Jun. 2011, pp. 1–4.

[18] H. Joshi, H. H. Sigmarsson, S. Moon, D. Peroulis, and W. J. Chappell, "High-Q fully reconfigurable tunable bandpass filter," *IEEE Trans. Microw. Theory Techn.*, vol. 57, no. 12, pp. 3525–3533, Dec. 2009.

[19] A. Fuduka, H. Okazaki, and S. Narahashi, "A novel compact reconfigurable quad-band power amplifier employing RF-MEMS switches," in *Proc. 36th Eur. Microw. Conf.*, Sep. 2006, pp. 344–347.

[20] H. Zhang, H. Gao, and G. Li, "Broad-band power amplifier with a novel tunable output matching network," *IEEE Trans. Microw. Theory Techn.*, vol. 53, no. 11, pp. 3606–3614, Nov. 2005.

[21] W. E. Neo, J. Lin, X. Liu, L. C. N. de Vreede, L. E. Larson, M. Spirito, M. Pelk, K. Buisman, A. Akhnoukh, A. de Graauw, and L. Nanver, "Adaptive multi-band multi-mode power amplifier using integrated varactor-based tunable matching network," *IEEE J. Solid-State Circuits*, vol. 41, no. 9, pp. 2166–2177, Sep. 2006.

[22] H. M. Nemati, J. Grahn, and C. Fager, "Band-reconfigurable LDMOS power amplifier," in *Proc. 40th Eur. Microw. Conf.*, Sep. 2010, pp. 978–981.

[23] K. Chen and D. Peroulis, "Design of adaptive highly efficient GaN power amplifier for octave-bandwidth application and dynamic load modulation," *IEEE Trans. Microw. Theory Techn.*, vol. 60, no. 6, pp. 1829–1839, Jun. 2012.

[24] Advanced Design System (ADS). ver. 9, Agilent Technol., Santa Clara, CA, 2009. [Online]. Available: http://www.agilent.com.

[25] H. M. Nemati, C. Fager, M. Thorsell, and H. Zirath, "High-efficiency LDMOS power amplifier design at 1 GHz using an optimized transistor model," *IEEE Trans. Microw. Theory Techn.*, vol. 57, no. 7, pp. 1647–1654, Jul. 2009.

[26] V. Carrubba, J. Lees, J. Benedikt, P. J. Tasker, and S. C. Cripps, "A novel highly efficient broadband continuous class-F RFPA delivering 74% average efficiency for an octave bandwidth," in *IEEE MTT-S Int. Microw. Symp. Dig.*, Jun. 2011, pp. 1–4.

[27] K. Chen and D. Peroulis, "Design of highly efficient broadband class-E power amplifier using synthesized lowpass matching networks," *IEEE Trans. Microw. Theory Techn.*, vol. 59, no. 12, pp. 3162–3173, Dec. 2011.

[28] X. Liu, L. P. B. Katehi, W. J. Chappell, and D. Peroulis, "Power handling of electrostatic MEMS evanescent-mode (EVA) tunable bandpass filters," *IEEE Trans. Microw. Theory Techn.*, vol. 60, no. 2, pp. 270–283, Feb. 2012.

[29] High Frequency Structure Simulator (HFSS). Ansoft Cooperation, Pittsburgh, PA, 2011. [Online]. Available: http://www.ansoft.com/products/hf/hfss/

[30] J. Kim, J. Kim, J. Moon, J. Son, I. Kim, S. Jee, and B. Kim, "Saturated power amplifier optimized for efficiency using self-generated harmonic current and voltage," *IEEE Trans. Microw. Theory Techn.*, vol. 59, no. 8, pp. 2049–2058, Aug. 2011.

[31] M. R. Hoque, T. Ahmad, T. McNutt, A. Mantooth, and M. M. Mojarradi, "Design technique of an on-chip, high-voltage charge pump in SOI," in *IEEE Int. Circuits Syst. Symp.*, Mar. 2006, pp. 133–136.

[32] V. Jimenez, J. Pons, M. Domingues, A. Bermejo, L. Castaner, H. Nieminen, and V. Ermolov, "Transient dynamics of a MEMS variable capacitor driven with a dickson charge pump," *Sens. Actuators A, Phys.*, vol. 128, no. 1, pp. 89–97, Mar. 2006.

[33] K. Chen, H. H. Sigmarsson, W. J. Chappell, and D. Peroulis, "Power handling of high-Q evanescent-mode tunable filters with integrated piezoelectric actuators," in *IEEE MTT-S Int. Microw. Symp. Dig.*, Jul. 2012, pp. 1–3.

[34] A. Sayed, A. A. Tanany, and G. Boeck, "5 W,0.35–8 GHz linear power amplifier using GaN HEMT," in *Proc. the 39th Eur. Microwave Conf.*, Sep. 2009, pp. 488–491.

Kenle Chen (S'10) received the Bachelor's degree in communication engineering from Xi'an Jiaotong University, Xi'an, China, in 2005, the Master's degree in electronics and information engineering from Peking University, Beijing, China, in 2008, and is currently working toward the Ph.D. degree at Purdue University, West Lafayette, IN.

From 2007 to 2008, he was with the Institute of Micro Electronics, National Key Laboratory of Micro/Nano Fabrication, Peking University, where his research focused on RF microelectromechanical systems (MEMS) switches, tunable filters, and vacuum packaging. He is currently with the School of Electrical and Computer Engineering and Birck Nanotechnology Center, Purdue University, where his research interests include broadband highly efficient PA design methodologies, adaptive PAs and transmitters, integration of PA and high-Q filter (co-design technique), and high-power failure mechanisms of microwave devices.

Mr. Chen was the recipient of the Second Place Award and Third Place Award of the Student High Efficiency Power Amplifier Design Competition, IEEE Microwave Theory and Techniques Society (IEEE MTT-S) International Microwave Symposium (IMS) in 2012 and 2011, respectively. He was also a recipient of 2012 IEEE MTT-S Graduate Research Fellowship.

Xiaoguang Liu (S'07–M'11) received the Bachelor's degree in electrical engineering from Zhejiang University, Hangzhou, China, in 2004, and the Ph.D. degree from Purdue University, West Lafayette, IN, in 2010.

He is currently an Assistant Professor with the Department of Electrical and Computer Engineering, University of California at Davis. His research interests include novel MEMS/nanoelectromechanical systems (NEMS) devices, high-Q tunable components for reconfigurable radio frontends, microwave/millimeter-wave/terahertz electronics, and biomedical applications of microwave/ultrasound technologies.

Dimitrios Peroulis (S'99–M'04) received the Ph.D. degree in electrical engineering from The University of Michigan at Ann Arbor, in 2003.

Since August 2003, he has been with Purdue University. He leads the Adaptive Radio Electronics and Sensors (ARES) team, which focuses on reconfigurable analog/RF electronics for adaptive communications, signal intelligence, and harsh-environment sensors. He has been a Principle Investigator (PI)/co-PI in over 40 projects funded by government agencies and industry in these areas. Since 2007, he has been a key contributor to the Defense Advanced Research Projects Agency (DARPA) Analog Spectral Processors (ASPs) (Phases I–III) project resulting in the first widely tunable (tuning range $>$3:1) pre-select radio filters with unprecedented quality factors ($Q > 1000$) and power handling (> 10 W) for high-frequency applications (1–30 GHz). A wide variety of reconfigurable filters with simultaneously adaptable features including frequency, bandwidth, rejection level, filter order, and group delay have been demonstrated over the past four years. His group recently codeveloped a ground-breaking concept of field programmable filter arrays (FPFAs). Inspired by FPGAs in digital systems, FPFAs are based on a sea of coupled resonators and multiple ports in order to enable reutilization of the same adaptive resonators to support diverse needs for dissimilar systems. Arbitrary operational modes and multiple operational channels may be created and reconfigured at will. Moreover, he has made significant advances in high-power high-efficient PAs and RF CMOS integrated circuits (ICs) with high-efficiency antennas. In the areas of sensors, he has also demonstrated the first wireless battery-free high-temperature MEMS sensors for health monitoring of sensitive bearings in aircraft engines. These sensors continuously monitor (RF identification (RFID) type) the true temperature of the bearing to over 300 °C or 550 °C (depending on the design) and wirelessly transmit it to a base station. These sensors are based on well-established silicon processing for low-cost high-yield manufacturing. They have demonstrated extremely robust operation for over 1B cycles and continuous loading for over three months without failure.

Prof. Peroulis and his team were the recipients of Third Place in the Student PA Design Competition, 2011 IEEE Microwave Theory and Techniques Society (IEEE MTT-S) International Microwave Symposium (IMS). In addition, a student design team led by Prof. B. Jung (lead) and himself (assistant team leader) at Purdue University was awarded the First Place Awards in Phases I and II of the 2007–2008 SRC/SIA IC Design Challenge by demonstrating high-efficiency chip-to-chip wireless links with U-band transceivers. Further advances led to bond-wire Yagi antenna arrays with efficiencies exceeding $>$80%.